Inorg. Chem. **2007**, *46*, 859–865

Stacking Design of Inverse Perovskites: The Systems $(Sr_{3-x}Ba_x)N)E$, E = Bi, Sb

Frank Gäbler[†,‡] and Rainer Niewa*[,†,‡]

Max-Planck-Institut für Chemische Physik fester Stoffe, Nöthnitzer Straße 40, 01187 Dresden, Germany, and Department Chemie, Technische Universität München, Lichtenbergstrasse 4, 85747 Garching, Germany

Received September 28, 2006

The first representatives of 4H ($BaMnO_3$-type structure, $P6_3/mmc$, $Z = 4$) and 9R ($BaMnO_3$-type structure, $R\bar{3}m$, $Z = 9$) inverse Perovskite phases are presented. The phases are obtained within the solid solutions $(Sr_{3-x}Ba_x)N)E$ with E = Bi, Sb. The crystal structures and homogeneity ranges were studied by combined X-ray and neutron diffraction as well as chemical analyses. The cubic Perovskite phase with Bi (Sb) is stable in the range of $0.00 \leq x \leq 0.90(5)$ ($0.00 \leq x \leq 1.30(5)$), the 4H variant is stable for $1.55(5) \leq x \leq 2.10(5)$ ($1.85(5) \leq x \leq 2.45(5)$), the 9R structure is stable for $2.50(2) \leq x \leq 2.55(2)$ ($2.56(2) \leq x \leq 2.60(2)$), and the 2H phase is stable for $2.75(5) \leq x \leq 3.00$ ($2.80(5) \leq x \leq 3.00$). Ba occupies preferable sites in the hexagonal stacking of close packed layers of alkaline earth metal ions and E^{3-}; Sr is mainly located in cubic stacked layers. The phase order upon going from cubic $(Sr_3N)E$ to 2H-type $(Ba_3N)E$ concomitant to the pronounced Sr/Ba partial order can, in general, be rationalized considering the Coulomb repulsion of nitride ions, as well as the size and charge density of the alkaline earth metal ions.

Introduction

The cubic Perovskite crystal structure is one of the most stable atomic arrangements for ternary and multinary compounds and, together with its distortion variants, is found for an overwhelming number of compounds.[1] Additionally, with certain bonding or atomic radii constraints, so-called hexagonal Perovskites, stacking variants of the cubic Perovskite, are known and constitute a large group of compounds with a multitude of interesting and useful properties. Inverse Perovskites result from interchange of crystallographic positions of anions by cations and vice versa. Although examples for inverse cubic Perovskites have been known since the early days of X-ray diffraction,[2,3] the numbers of "normal" Perovskites and hexagonal/trigonal stacking or distortion variants are unequaled. Until recently, only cubic inverse Perovskites, one distortion variant thereof, and examples for hexagonal Perovskites with a 2H structure were known.[4−10]

Ternary nitrides of the general composition $(Ca_3N)E$ have been known for a couple of years. The compounds crystallize in a cubic inverse Perovskite-type crystal structure (E = Tl, Ge, Sn, Pb, Sb, Bi, and Au) or in an orthorhombic distortion variant thereof (E = P, As).[4−7]Additionally, the Mg compounds $(Mg_3N)E$ (E = As, Sb)[8] were reported and crystallize in a cubic inverse Perovskite-type crystal structure. Recent reports deal with ternary nitrides of the composition $(A_3N_x)E$ with A = Sr, Ba and E = Sn, Pb ($0.66 \leq x \leq 0.82$), Sb, and Bi ($x = 1$).[9,10] The compounds of the composition $(Ba_3N_x)E$ and $(Sr_3N_x)E$ (E = Sn, Pb) crystallize in cubic inverse

* To whom correspondence should be addressed. Tel.: ++49 89/289-13098. Fax: ++49 89/289-13762. E-mail: rainer.niewa@ch.tum.de.
† Max-Planck-Institut für Chemische Physik fester Stoffe.
‡ Technische Universität München.

(1) Villars, P.; Calvert, L. D. *Pearson's Handbook of Crystallographic Data for Intermetallic Phases*, 2nd ed.; ASM International: Materials Park, OH, 1991.
(2) Brill, R. *Z. Kristallogr.* **1928**, *68*, 379−384.
(3) Morral, F. R. *J. Iron Steel Ind.* **1934**, *130*, 419−427.
(4) Jäger, J.; Stahl, D.; Schmidt, P. C.; Kniep, R. *Angew. Chem.* **1993**, *105*, 738−739; *Angew. Chem., Int. Ed. Engl.* **1993**, *32*, 709−710.
(5) Chern, M. Y.; Vennos, D. A.; DiSalvo, F. J. *J. Solid State Chem.* **1992**, *96*, 415−425.
(6) Niewa, R.; Schnelle, W.; Wagner, F. R. *Z. Anorg. Allg. Chem.* **2001**, *627*, 365−370.
(7) Chern, M. Y.; DiSalvo, F. J.; Parise, J. B.; Goldstone, J. A. *J. Solid State Chem.* **1992**, *96*, 426−435.
(8) Chi, E. O.; Kim, W. S.; Hur, N. H.; Jung, D. *Solid State Commun.* **2002**, *121*, 309−312.
(9) Gäbler, F.; Kirchner, M.; Schnelle, W.; Schmitt, M.; Rosner, H.; Niewa, R. *Z. Anorg. Allg. Chem.* **2005**, *631*, 397−402.
(10) Gäbler, F.; Kirchner, M.; Schnelle, W.; Schwarz, U.; Schmitt, M.; Rosner, H.; Niewa, R. *Z. Anorg. Allg. Chem.* **2004**, *630*, 2292−2298.

10.1021/ic061863h CCC: $37.00
Published on Web 01/05/2007

Table 1. Results of Chemical Analyses in Weight % and Resultant Compositions

phase	*w*(Ba)	*w*(Sr)	*w*(Bi)	*w*(N)	*w*(O)	analytical composition	composition from structure refinements
cubic	12.39(4)	43.7(1)	40.5(3)	2.54(5)	0.12(1)	$(Sr_{2.57(3)}Ba_{0.46(1)}N_{0.94(2)}O_{0.03(1)})Bi$	
cubic	24.22(7)	32.5(6)	38.8(5)	2.2(3)	0.15(2)	$(Sr_{2.00(6)}Ba_{0.95(2)}N_{0.86(13)}O_{0.05(1)})Bi$	
4H	41.5(6)	19.7(2)	36.2(5)	2.3(1)	<0.01	$(Sr_{1.30(3)}Ba_{1.75(5)}N_{0.96(5)})Bi$	$(Sr_{1.3(1)}Ba_{1.7}N)Bi$
4H	47.8(2)	14.69(7)	35.6(3)	2.27(9)	<0.01	$(Sr_{0.98(2)}Ba_{2.04(2)}N_{0.95(5)})Bi$	$(Sr_{1.1(1)}Ba_{1.9}N)Bi$
9R	57.8(4)	6.8(1)	34.8(2)	2.4(1)	<0.01	$(Sr_{0.46(1)}Ba_{2.53(2)}N_{1.02(2)})Bi$	$(Sr_{0.8(1)}Ba_{2.2}N)Bi$
4H	56.2(13)	15.3(1)	22.8(5)	2.6(1)	<0.01	$(Sr_{0.93(1)}Ba_{2.19(5)}N_{0.97(5)})Sb$	$(Sr_{1.13(6)}Ba_{1.87}N)Bi$
4H	62.1(7)	10.3(1)	23.0(3)	2.7(3)	0.3(1)	$(Sr_{0.62(1)}Ba_{2.39(3)}N_{1.02(12)}O_{0.11(4)})Sb$	

Perovskite-type structures with a nitride deficiency and show metallic properties. The semiconducting compounds $(Sr_3N)E$ with E = Sb, Bi also crystallize in cubic inverse Perovskite-type structures, while the structures of $(Ba_3N)E$ correspond to inverse 2H Perovskites ($BaNiO_3$-type). We present the gradual structural transition from cubic to 2H Perovskite via intermediate stacking variants within the solid solution systems $(Sr_{3-x}Ba_xN)Bi$ and $(Sr_{3-x}Ba_xN)Sb$ and try to rationalize the obtained crystal structures in dependence of chemical compositions and order schemes of the alkaline earth metal species.

Experimental Details

Synthesis and Characterization. All manipulations were carried out in an argon filled glovebox ($p(O_2, H_2O) < 0.1$ ppm). For the preparation of single-phase samples bismuth (Chempur 99.999%) or antimony (Chempur 99.999%) and strontium or barium (Alfa Aesar 99.9%) were fused in an arc furnace operated in argon (Air Liquid 5.0, additionally purified by passing over molsieve, Roth 3 Å, and BTS catalyst, Merck). The resulting metallic reguli typically were two-phase mixtures of A_5E_3 and A. No phases of A_3E with A = Sr, Ba and E = Bi, Sb are known according to the available phase diagrams.[11] In a second step, the metallic reguli were heated in nitrogen of ambient pressure to maximum temperatures of 1073 K or 1148 K for E = Sb or Bi, respectively. All quaternary nitrides with the general composition of $(Sr_{3-x}Ba_xN)E$ (E = Bi, Sb) were obtained as grayish-black powders, which are sensitive to water and moisture.

Chemical Analyses. Chemical analyses of N and O were carried out on representative single-phase products using the hot-extraction technique on a LECO analyzer TC-463 DR. Quantitative analyses of Sr, Ba, Sb, and Bi were performed using an ICP-OES (Varian Vista RL). All values are averages of at least three independent measurements. The results of the measurements are summarized in Table 1.

Crystal Structure Determination and Refinements. The quaternary nitrides were characterized by X-ray powder diffraction using an imaging plate Guinier camera equipped with a germanium monochromator (HUBER diffraction, Cu $K\alpha_1$ radiation, 6 × 15 min scans, $8° \le 2\Theta \le 100°$). The samples were loaded between two polyimide foils in an aluminum cell with a rubber seal to exclude moisture. Comparison of the first and the final scan did not indicate significant hydrolysis during the measurement procedure. Homogeneity ranges were determined from careful inspections of X-ray diffraction patterns; standard deviations refer to the grid patterns of Sr/Ba ratios in the preparation experiments, that is, to the minimal composition differences in the different single preparation experiments.

Neutron powder diffraction data on microcrystalline samples of $(Sr_{1.3}Ba_{1.7}N)Bi$, $(Sr_{1.0}Ba_{2.0}N)Bi$, $(Sr_{0.5}Ba_{2.5}N)Bi$, and $(Sr_{0.9}Ba_{2.1}N)Sb$ were gathered at the E9 powder diffractometer at BerII, HMI Berlin, Germany. The samples were contained in separate gas-tight vanadium cylinders (diameter 6 mm, length 51 mm, wall thickness 0.15 mm). The structures were refined simultaneously on the basis of both powder X-ray diffraction and neutron diffraction patterns with weighted contributions. Figures 1−4 depict the experimental diffraction patterns (Figures 1a, 2a, 3a, and 4a, neutron diffraction; Figures 1b, 2b, 3b, and 4b, X-ray diffraction) together with the calculated profiles and the difference curves of the observed and the simulated patterns as determined by least-squares refinements (program package FULLPROF[12]). For one sample ($(Sr_{0.9}Ba_{2.1}N)Sb$), a neutron diffraction pattern at 2 K was taken. No significant change in the pattern was observed, which indicates no structural change (e.g., distortion) at lower temperatures.

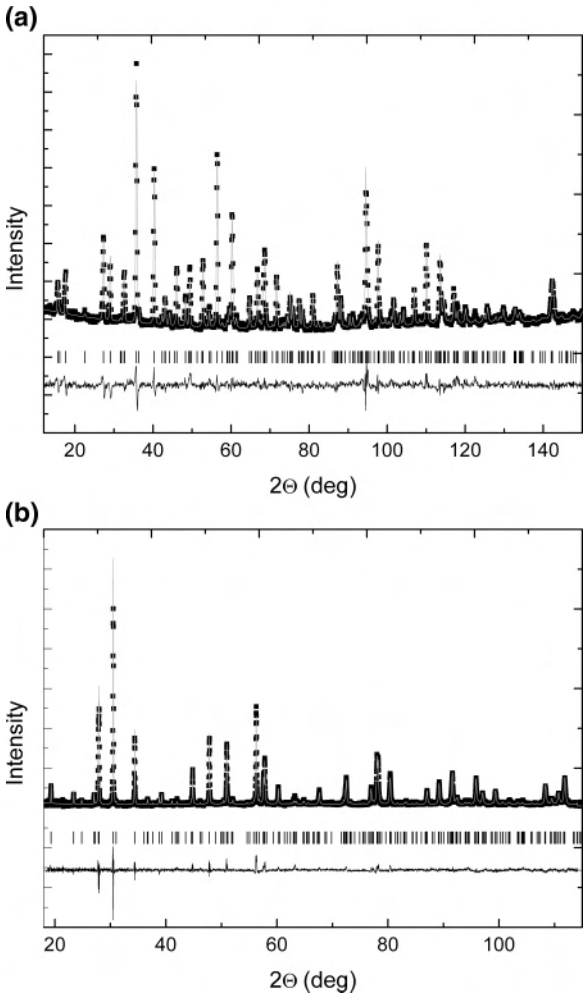

Figure 1. $(Sr_{1.0}Ba_{2.0}N)Bi$ (4H Perovskite): (a) neutron diffraction pattern and (b) X-ray powder diffraction pattern. The measured data are shown as points, the continuous line represents the calculated profile, and the lower line shows the difference between the calculated and the observed intensities. The tick marks below the data indicate positions of possible Bragg reflections.

(11) Massalski, T. B., Ed. *Binary Alloy Phase Diagrams*, 2nd ed.; ASM International: Materials Park, OH, 1990.

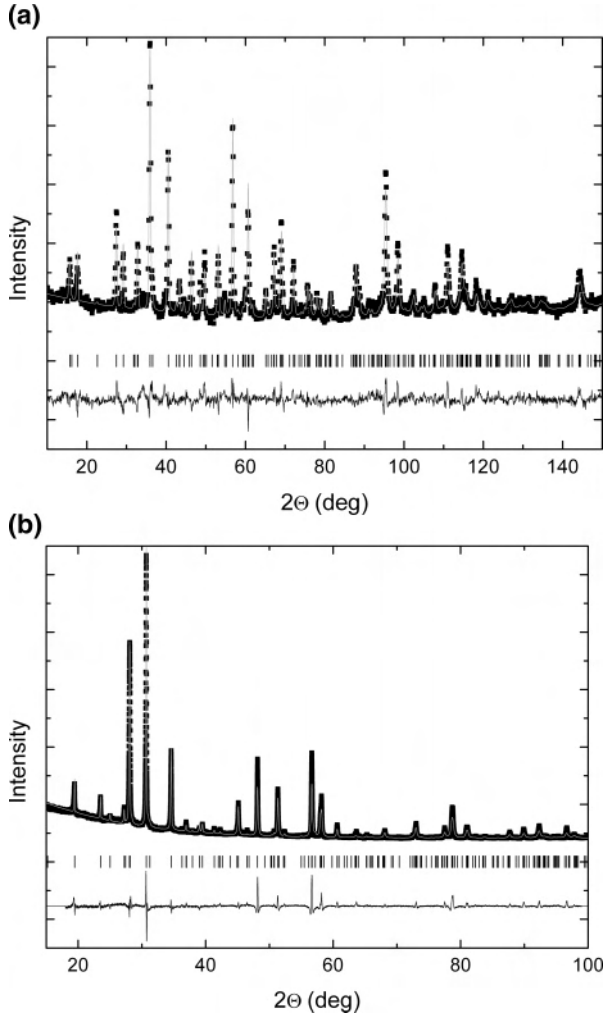

Figure 2. $(Sr_{1.3}Ba_{1.7}N)Bi$ (4H Perovskite): (a) neutron diffraction pattern and (b) X-ray powder diffraction pattern. The measured data are shown as points, the continuous line represents the calculated profile, and the lower line shows the difference between the calculated and the observed intensities. The tick marks below the data indicate positions of possible Bragg reflections.

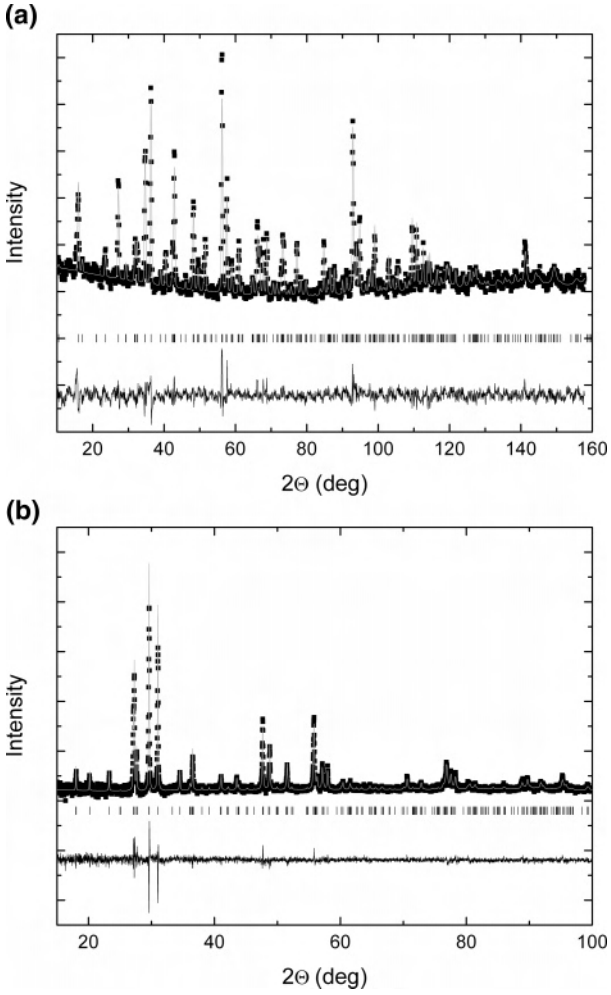

Figure 3. $(Sr_{0.5}Ba_{2.5}N)Bi$ (9R Perovskite): (a) neutron diffraction pattern and (b) X-ray powder diffraction pattern. The measured data are shown as points, the continuous line represents the calculated profile, and the lower line shows the difference between the calculated and the observed intensities. The tick marks below the data indicate positions of possible Bragg reflections.

Magnetic Susceptibility. The magnetization of powder samples (sealed in silica tubes, 400 mbar He) was measured in a SQUID magnetometer (MPMS XL-7, Quantum Design) in external magnetic fields ranging from 70 kOe to 10 Oe between 1.8 and 400 K. All samples are diamagnetic with only very small paramagnetic and ferromagnetic impurities (lower ppm range).

Electrical Resistivity. Measurements of the electrical conductivity were performed on powders pressed in a sapphire die in a four contact direct current van der Pauw setup between 50 and 350 K. The temperature dependence for all samples indicates semiconducting properties.

Results and Discussion

As already noted, ternary compounds $(A_3N)E$ with A = Sr, Ba and E = Bi, Sb adopt inverse Perovskite-type arrangements with nitrogen in octahedral coordination with six alkaline earth metal ions and group 15 element anions in the resulting voids of this framework. Cubic Perovskite nitrides and distortion variants thereof with group 15 elements have previously been reported for the systems $(Ca_3N)E$ with E = P, As, Sb, and Bi and $(Mg_3N)E$ with E = As, Sb.[5,7,8] While $(Sr_3N)Sb$ and $(Sr_3N)Bi$ represent cubic Perovskites ($Pm\bar{3}m$, $Z = 1$), $(Ba_3N)Sb$ and $(Ba_3N)Bi$ crystallize in a hexagonal Perovskite variant of the $BaNiO_3$ structure type ($P6_3/mmc$, $Z = 2$).[9] On substitution of strontium by barium, the transition from cubic to 2H Perovskite develops gradually. Within the quasi-binary systems $(Sr_3N)E$ and $(Ba_3N)E$, a structural change from the cubic to the hexagonal 2H Perovskite conducts via a 4H variant ($BaMnO_3$-type structure, $P6_3/mmc$, $Z = 4$) and a 9R variant ($BaMnO_3$-type structure, $R\bar{3}m$, $Z = 9$). We could not obtain any indications for further stacking variants. Apparently, the energy difference of partially ordered structures with even longer repeating units compared to that of the 2H structure with Sr and Ba disordered on one crystallographic site at the reaction temperatures is too small to favor the formation of such larger

(12) (a) Roisnel, T.; Rodriguez-Carvajal, J. *WinPLOTR*, version May, 2000; *Materials Science Forum*, Proceedings of the 7th European Powder Diffraction Conference; Barcelona, Spain, 2000; p 188. (b) Rodriguez-Carjaval, J. *FULLPROF.2k*, version 1.6; 2000; Laboratoire Léon Brillouin, 2000; *Abstract of Satellite Meeting on Powder Diffraction*, Congress of the International Union of Crystallography; Toulouse, France, 1990; p 127.

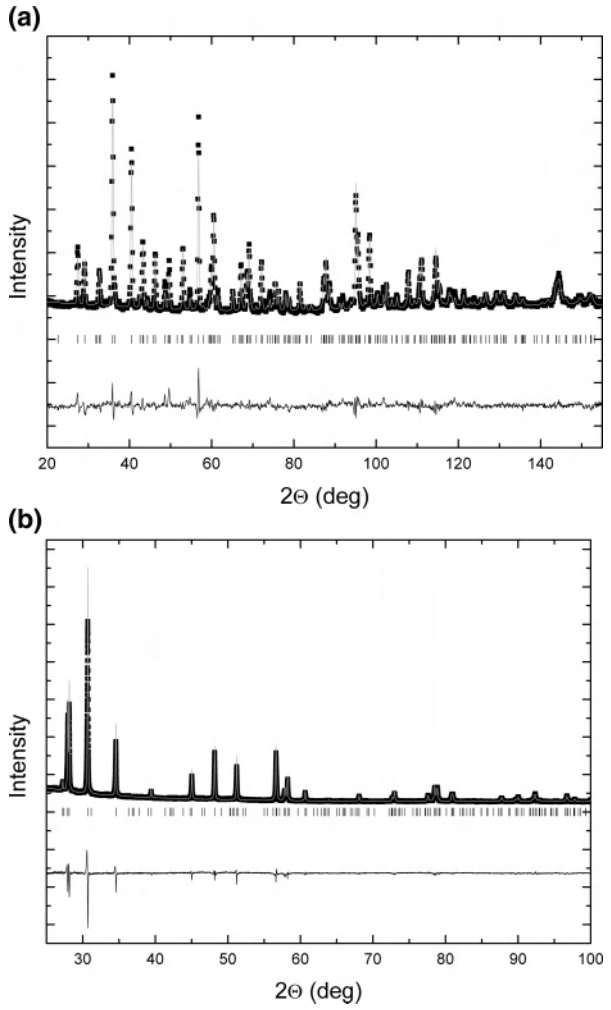

Figure 4. $(Sr_{0.9}Ba_{2.1}N)Sb$ (4H Perovskite): (a) neutron diffraction pattern and (b) X-ray powder diffraction pattern. The measured data are shown as points, the continuous line represents the calculated profile, and the lower line shows the difference between the calculated and the observed intensities. The tick marks below the data indicate positions of possible Bragg reflections.

superstructures. The crystal structures of the cubic Perovskite and the 4H, 9R, and 2H variants are depicted in Figure 5. While the cubic Perovskite can be described as consisting of a three-dimensional framework of vertex-linked A_6N octahedra with an E^{3-} ion in large cuboctahedrally coordinated voids, those octahedra are face-sharing in the 2H-Perovskite variant. In the 4H structure, blocks of two face-sharing octahedra are interlinked via all six terminal corners to a three-dimensional framework; in the 9R structure, these blocks consist of three face-sharing octahedra. In a different description based on stacking of hexagonal A_3E layers, the stacking sequence ...ABC... corresponds to the cubic Perovskite (Jagodzinski notation *c*); ...ABAC... corresponds to the 4H structure (*hc*); ...ABABCBCAC... corresponds to the 9R variant (*hhc*); and ...AB... corresponds to the 2H Perovskite (*h*).

In both quaternary systems $(Sr_{3-x}Ba_xN)E$ (E = Bi, Sb), the homogeneity ranges of the Perovskite structure types (cubic, 4H, 9R, and 2H) were investigated in detail. For a temperature of 1148 K (Bi) and 1073 K (Sb) the homogeneity ranges are given in Table 2. As one might expect, the

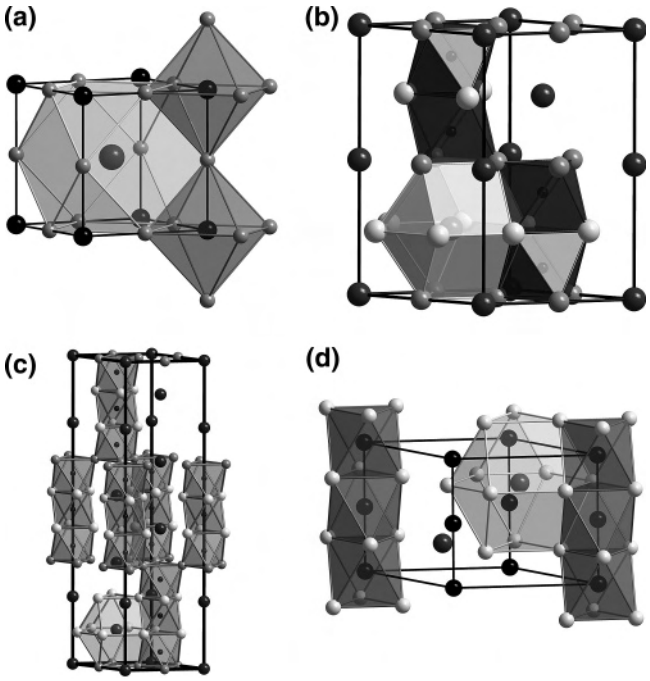

Figure 5. Structure representations of compounds $(Sr_{3-x}Ba_xN)E$ (E = Sb, Bi) with (a) a cubic Perovskite-type structure ($x = 0$), (b) a 4H $BaMnO_3$-type structure ($x \approx 2.0$), (c) a 9R $BaRuO_3$-type structure ($x \approx 2.5$), and (d) a 2H $BaNiO_3$-type structure ($x = 3.0$). Small black spheres in centers of octahedra, N; large black spheres, E = Sb, Bi; gray spheres, mainly Sr; light gray spheres, mainly Ba. Sr is predominantly located at vertex-sharing sites of (A_6N) octahedral (gray); Ba is at face-sharing positions.

Table 2. $(Sr_{3-x}Ba_xN)Bi$ ($T = 1148$ K) and $(Sr_{3-x}Ba_xN)Sb$ ($T = 1083$ K): Homogeneity Ranges of Different Phases

phase	$(Sr_{3-x}Ba_xN)Bi$	$(Sr_{3-x}Ba_xN)Sb$
cubic	$0.00 \le x \le 0.90(5)$	$0.00 \le x \le 1.30(5)$
4H	$1.55(5) \le x \le 2.10(5)$	$1.85(5) \le x \le 2.45(5)$
9R	$2.50(2) \le x \le 2.55(2)$	$2.56(2) \le x \le 2.60(2)$
2H	$2.75(5) \le x \le 3.00$	$2.80(5) \le x \le 3.00$

homogeneity ranges are separated by two-phase regions of various widths. These data are graphically presented in Figures 6 and 7. For better comparability, the unit cell parameters are recalculated to hexagonal settings and normalized to two octahedra in the [001] direction of the resulting hexagonal axes (cubic, $a' = a/\sqrt{2}$, $c' = 2a/\sqrt{3}$; 4H, $a' = a/2$, $c' = c/2$; 9R, $a' = a/2$, $c' = 2c/9$; 2H, $a' = a/2$, $c' = c$). The c/a ratios refer to these values. Figures 6a and 7a and Figures 6b and 7b plot the unit cell parameters and the volumes per formula unit as functions of the Ba content, respectively. The homogeneity ranges of the antimony-containing phases are shifted toward higher barium content when compared with those of the bismuth-containing phases. This trend in homogeneity ranges results from different polarizabilities and ionic sizes of bismuth and antimony. Within two-phase regions, the unit cell parameters and volumes are constant as expected. Some scatter and deviations are due to experimental limitations. This is particularly true for the minority phases close to the boarders of homogeneity ranges, since the diffraction lines in X-ray patterns naturally get weak and are difficult to determine. Within the homogeneity ranges of the phases, the unit cell volumes increase linearly with increasing barium content

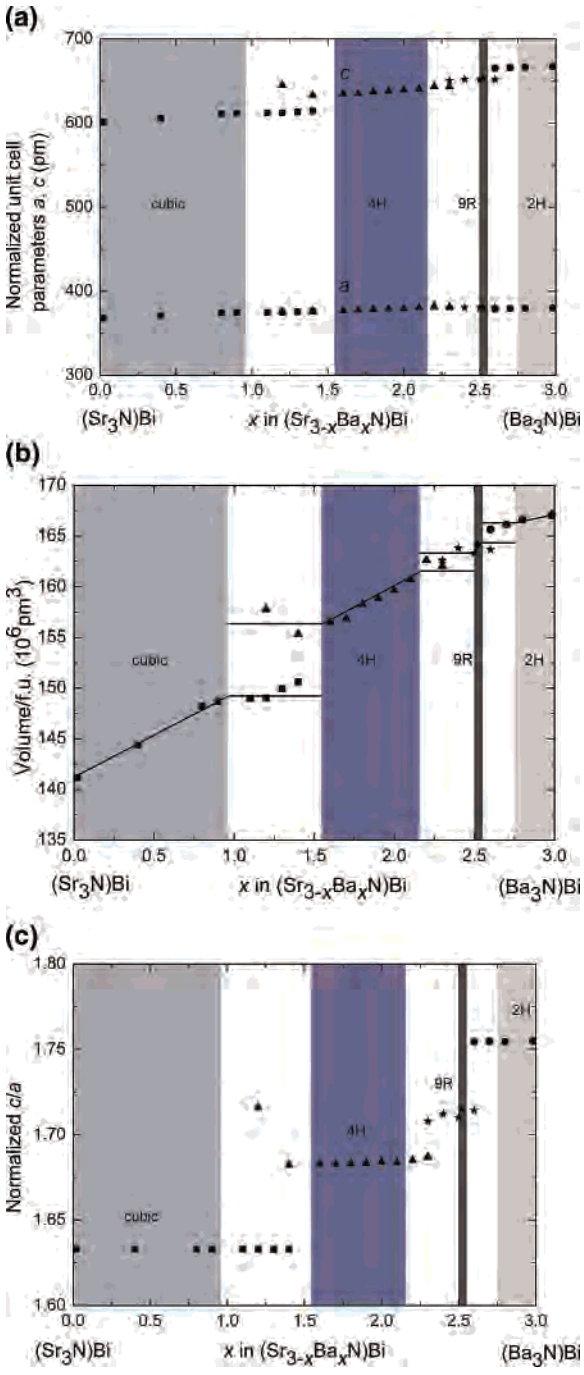

Figure 6. Dependence of (a) normalized unit cell dimensions, (b) volumes per formula unit, and (c) the normalized *c*/*a* ratio of phases $(Sr_{3-x}Ba_x)Bi$ on *x* from experiments at 1148 K. For information on the calculation of these values from the unit cell parameters see the main text body.

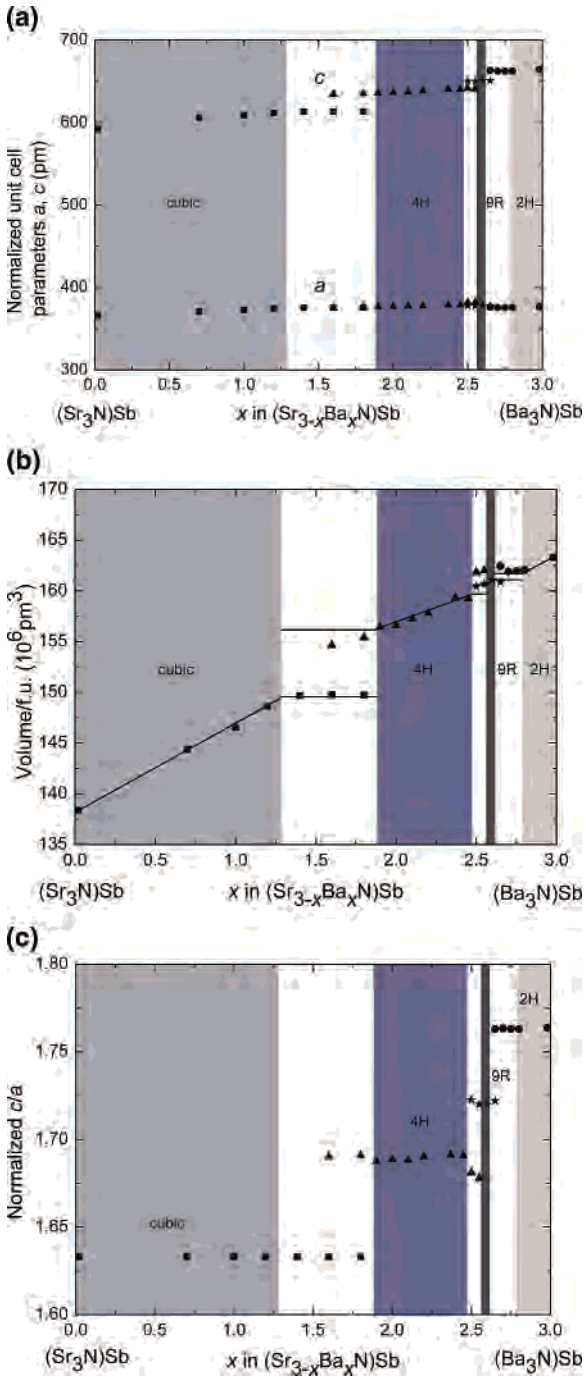

Figure 7. Dependence of (a) normalized unit cell dimensions, (b) volumes per formula unit, and (c) the normalized *c*/*a* ratio of phases $(Sr_{3-x}Ba_x)Sb$ on *x* from experiments at 1083 K. For information on the calculation of these values from the unit cell parameters see the main text body.

following the rule of Vegard. Figures 6c and 7c present the same data as the *c*/*a* ratio normalized to the value for close packings. While the cubic Perovskites are constrained to the ideal *c*/*a* ratio of a closed packing, the 4H, 9R, and 2H Perovskite show a deviation from the ideal *c*/*a* proportion to larger values. These differences result from an increased repulsive $N^{3-}-N^{3-}$ Coulomb interaction in the hexagonal variants because of shorter N−N distances as compared to those of the cubic Perovskite (see Table 3). The deviation from the ideal *c*/*a* value increases with an increasing number of face-sharing octahedra and is partially compensated by elongation of the octahedra in the [001] direction ($V \propto a^2c$, compression in *a* direction), partially by displacement of the nitride ions in the terminal octahedra of every block of face-sharing octahedra from the central position (4H and 9R). The latter fact can be taken from the Rietveld refinement results. Selected distances in the Bi-containing phases are gathered in Table 3.

Naturally, phases with significant homogeneity ranges exhibit defects, disorder, or, in the present case, partial ordering of the two different alkaline earth metal constituents. To gain insight into the mechanism of the transition from

Table 3. Selected Distances of the Different Perovskite Structure Types in the Quaternary System $(Sr_{3-x}Ba_xN)Bi$

phase	compound	*d*(Ba−N)	*d*(Sr−N)	*d*(Bi−*A*)	*d*(N−N)
cubic	$(Sr_3N)Bi$[10]		260.346(4)	368.18(1)	520.691(8)
4H	$(Sr_{1.3}Ba_{1.7}N)Bi$	270.9(4)[a]	262.4(4)[a]	377.7(5)	343.3(9)
4H	$(Sr_{1.0}Ba_{2.0}N)Bi$	271.0(4)[a]	264.7(4)[a]	380.0(3)	343.2(9)
9R	$(Sr_{0.48}Ba_{2.52}N)Bi$	268.3(5)[a]	268.8(8)[a]	380.9(3)	334(1)
2H	$(Ba_3N)Bi$[10]	267.7(1)		380.7(1)	334.047(5)

[a] Distances (in pm) that exhibit a majority component of the alkaline earth element but are not pure distances A−N.

Table 4. Selected Data of Joint Rietveld Refinements Based on X-ray and Neutron Powder Diffraction Data on Phases in the Homogeneity Range of the 4H Perovskite

composition	$(Sr_{1.3}Ba_{1.7}N)Bi$		$(Sr_{1.0}Ba_{2.0}N)Bi$		$(Sr_{0.9}Ba_{2.1}N)Sb$	
	X-ray diffraction	neutron diffraction	X-ray diffraction	neutron diffraction	X-ray diffraction	neutron diffraction
no. structural parameters	11		11		11	
radiation [pm]	Cu $K\alpha_1$	179.73(3)	Cu $K\alpha_1$	179.795(9)	Cu $K\alpha_1$	179.795(9)
Rietveld						
unit cell parameter *a* [pm]	755.18(5)		759.70(2)		754.09(4)	
unit cell parameter *c* [pm]	1270.67(8)		1279.53(2)		1273.99(6)	
Guinier						
unit cell parameter *a* [pm]	755.19(9)		759.34(7)		754.9(1)	
unit cell parameter *c* [pm]	1270.5(3)		1279.0(1)		1274.5(2)	
space group	$P6_3/mmc$		$P6_3/mmc$		$P6_3/mmc$	
2θ range [deg]	18−99	10−151.5	18.5−114.2	10−151.8	25−100.5	10−140
$R_{profile}$, R_{Bragg}	0.072, 0.080	0.053, 0.088	0.095, 0.094	0.050, 0.066	0.109, 0.087	0.068, 0.091

Table 5. Fractional Positional and Isotropic Displacement Parameters (in 10^{-4} pm^2) of Rietveld Refinements of X-ray and Neutron Powder Diffraction Data on $(Sr_{1.3}Ba_{1.7}N)Bi$ (Upper Values), $(Sr_{1.0}Ba_{2.0}N)Bi$ (Middle Bold Values), and $(Sr_{0.9}Bi_{2.1}N)Sb$ (Lower Italic Values)

site	atom	*x*	*y*	*z*	occupation	B_{iso}
4*f*	N	1/3	2/3	0.6149(5)	1	0.9(1)
				0.6159(5)		**1.0(1)**
				0.6161(4)		*1.00(8)*
2*a*	*E*(1)	0	0	0	1	1.0(2)
						1.3(1)
						0.7(2)
2*c*	*E*(2)	1/3	2/3	1/4	1	0.7(2)
						0.82(9)
						1.0(2)
6*h*	Ba(1)/Sr(1)	0.8269(6)	−*x*	1/4	0.84(2)/0.16	0.7(1)
		0.8261(4)			**0.88(2)/0.12**	**1.43(7)**
		0.8275(5)			*0.88(2)/0.12*	*1.10(9)*
6*g*	Ba(2)/Sr(2)	1/2	0	0	0.29(3)/0.71	1.5(1)
					0.38(2)/0.62	**1.8(1)**
					0.36(2)/0.62	*2.0(1)*

Table 6. Results of Rietveld Refinements of X-ray and Neutron Powder Diffraction Data on $(Sr_{0.5}Ba_{2.5}N)Bi$

		X-ray diffraction	neutron diffraction
no. of structural parameters		14	
radiation [pm]		Cu $K\alpha_1$	179.73(2)
unit cell parameter *a* [pm]	Rietveld	762.03(7)	
unit cell parameter *c* [pm]		2936.1(2)	
unit cell parameter *a* [pm]	Guinier	761.58(7)	
unit cell parameter *c* [pm]		2934.9(3)	
space group		$R\bar{3}m$	
2θ range [deg]		15−100	10−157.8
$R_{profile}$, R_{Bragg}		0.072, 0.087	0.079, 0.096

cubic Perovskite via the various hexagonal stacking variants on increasing barium content, the phases were studied with X-ray and neutron powder diffraction. The results from Rietveld refinements are summarized in Tables 4−7. The refinement results are graphically represented in Figures 1−4. In the 4H and 9R Perovskites, the face sharing of A_6N octahedra is realized preferably by A = Ba, while vertex-linking positions are occupied preferably by strontium (see

Table 7. Fractional Positional and Isotropic Displacement Parameters (in 10^{-4} pm^2) of Rietveld Refinements of X-ray and Neutron Powder Diffraction Data on $(Sr_{0.5}Ba_{2.5}N)Bi$

site	atom	*x*	*y*	*z*	occupation	B_{iso}
6*c*	N	0	0	0.3860(5)	1	1.1(2)
3*b*	N	0	0	1/2	1	0.7(3)
3*a*	Bi(1)	0	0	0	1	0.8(4)
6*c*	Bi(2)	0	0	0.2248(3)	1	0.9(3)
18*h*	Ba(1)/Sr(1)	0.1590(7)	−*x*	0.5570(2)	0.86(4)/0.14	1.3(2)
9*e*	Ba(2)/Sr(2)	1/2	0	0	0.42(5)/0.58	1.8(3)

Figure 5). Similar to the case of inverse Ruddlesden−Popper phases[13] $((Ba_{0.62(1)}Sr_{0.38})_{10}N_2O)Bi_4$ and $((Ba_{0.78(1)}Sr_{0.22})_4O)Bi_2$, we can explain such a partial ordering scheme with ionic size, polarizability, and space filling reasons. Upon going from $(Sr_3N)E$ to $(Ba_3N)E$, the closed packing of Sr and E is expanded by the substitution of strontium by barium. The resulting increased distance A−N causes decreasing attractive Coulomb interactions between Sr^{2+} and N^{3-}. A closer packing of A and E in a Ba-richer region is achieved by a transition of the crystal structure from cubic to the stacking variants 4H, 9R, and finally 2H Perovskite. The preference of occupation of the face-sharing positions of A_6N octahedra with Ba not only increases the distance between nitride species compared with an alternative occupation by Sr but also shields the negative charges more efficiently. The discussed structure characteristics of the hexagonal stacking variants 4H and 9R are supported by joint Rietveld refinements of neutron powder diffraction patterns and their corresponding X-ray powder diffraction patterns of $(Sr_{1.3}Ba_{1.7}N)Bi$, $(Sr_{1.0}Ba_{2.0}N)Bi$, $(Sr_{0.5}Ba_{2.5}N)Bi$, and $(Sr_{0.9}Ba_{2.1}N)Sb$. Moreover, the resulting compositions are in excellent agreement with the data from chemical analyses (see Experimental Details and Table 1). A neutron diffraction pattern of $(Sr_{0.9}Ba_{2.1}N)Sb$ at 2 K did not show any significant

(13) Gäbler, F.; Prots, Y.; Niewa, R. *Z. Anorg. Allg. Chem.* **2007**, *633*, 93−97.

change compared to the respective pattern taken at ambient temperature. Apparently, no structural change occurs upon cooling down to this temperature.

Finally, all studied phases can be rationalized exclusively to contain closed shell particles according to $(A^{2+})_3N^{3-}E^{3-}$. Correspondingly, measurements of the electrical resistivity and the magnetic susceptibility reveal semiconducting and diamagnetic behavior with only small dependence of these properties on the actual composition or on the crystal structure. Similar behavior was previously obtained for the ternary compounds $(A_3N)E$ (A = Sr, Ba; E = Sb, Bi).[9,10] No systematic trends could be determined from the experimental data.

Conclusions

The first representatives of 4H and 9R inverse Perovskite phases are presented. The phases are obtained in the solid solution series $(Sr_{3-x}Ba_x)N)E$ with E = Bi, Sb. The crystal structures and homogeneity ranges were studied by combined X-ray and neutron diffraction as well as chemical analyses. The phase order upon going from cubic $(Sr_3N)E$ via 4H- and 9R-type phases to 2H-type $(Ba_3N)E$ concomitant to the pronounced Sr/Ba partial order can, in general, be rationalized considering the Coulomb repulsion of nitride ions competing with Coulomb attractions in closely packed structures.

Acknowledgment. We thank Steffen Hückmann for the collection of the X-ray powder diffraction data, Anja Völzke for performing the chemical analyses, Ralf Koban and Dr. Walter Schnelle for operating the SQUID and performing the resistivity measurements, and Prof. Dr. R. Kniep for his constant interest and support. The neutron diffraction data collection by Dr. Gudrun Auffermann at the E9 diffractometer operated by Dr. Daniel Többens is gratefully acknowledged. This work was supported by the Max-Planck-Gesellschaft and the Elitenetzwerk Bayern within the Advanced Materials Science program.

Supporting Information Available: Rietveld refinement details. This material is available free of charge via the Internet at http://pubs.acs.org.

IC061863H